ADVANCED FUNCTIONAL MATERIALS
www.afm-journal.de

A Flexibly Function-Oriented Assembly Mechanical Metamaterial

Chengbin Yue, Wei Zhao, Fengfeng Li, Bingxun Li, Liwu Liu, Yanju Liu,* and Jinsong Leng*

Based on the snap-through instability, the pursuit for mechanical metamaterials with flexible functional applications and the ability to combine with information has been the Holy Grail for structural scientists. Here, the function/application-oriented bistable unit motifs (UMs) are developed by an elaborately architectural design inspired by the hind leg of the frog in jumping, and a corresponding assembled strategy is proposed. Three functional applications derived from their progressive evolutions. The first is the construction of on-demand assemblable mechanical curves, including multi-stage vibration isolation, recoverable energy absorption, and energy dissipation along with integrated vibration isolation and energy dissipation characteristics. The second is the development of mechanic and temperature double pattern encryption strategy using bistability and shape memory programmability, resulting in 4^n encryption and decryption modes for n-bit encryption devices. Finally, five non-volatile basic mechanical logic gates and a universal combinatorial half-adder are built, affording guidance to unconventional computing devices with logic functions.

1. Introduction

Snap-through instability is popularly present in natural biological systems to ensure survival.[1,2] For example, the Venus flytrap leaf can achieve fast capture by switching rapidly between two stable equilibrium states (opened convex shape and closed concave shape),[3,4] as well as other prominent examples (e.g., the rapidly closing beak of hummingbirds,[5] the extremely fast strike of *Odontodactylus scyllarus*,[6] and the spine of a cheetah running at high speed[7]). Recently, significant progress has been made to integrate mechanical instabilities in design to generate bistability,[2,8] multi-stability,[9,10] or programmable behavior.[11,12] These properties are applicable to flexible systems such as soft robotics, achieving amplified force output and faster response to overcome the inherent limitations of soft materials.[13–15] Moreover, the structural bi-/multistability have been also exploited to develop energy absorption,[16–19] energy dissipation,[20–23] and shape reconfiguration structures.[24–27] Despite a multitude of explorations by engineers, the utilization of snap-through instability still shows a lack of flexible functional applications and the ability to combine with information. There are mainly three limitations: i) single deformation mode for unit motifs, ii) limited design space, and iii) impediments for integrating deformation motions and information. To break through these limitations, Mei et al.[28] proposed a reprogrammable mechanological metamaterials, which can excellently realize universal combinatorial logic and sequential logic. Zhang et al.[29] designed the scalable X-shaped tristable structures by exploiting kirigami microstructures, demonstrating extraordinary capabilities of multidirectional multistability. Their potential application in ternary metalogic operation was validated. Liu et al.[30] suggested the extraordinary construction and adjustment of mechanical logic gates on the basis of stacked Miura-ori-variant structures. The implementation of various complex logic operations without increasing the structural complexity demonstrates its outstanding computational power. Furthermore, they presented a new multistable origami computing framework that can perform high-level calculative missions without a logic gate network.[31] Charles et al.[32] integrated and programmed combinational logic circuits into the mechanical metamaterials using a robust strategy, revealing the relationship between Boolean mathematics and kinematically reconfigurable structures. The works mentioned above have provided tremendous guidance for our research.

Moreover, recent developments in metamaterials have introduced a flexible and practical assembly strategy that is not limited to manufacturing technology and can integrate multiple material systems.[33–36] How to cleverly utilize bistable units based on assembly strategies has become the cornerstone of expanding functional application fields. However, traditional bistable elements, such as constrained inclined[37]/curved[23,38] beams and 3D shallow domes,[39] have limited deformation modes and single functional characteristics, limited by their fixed boundary conditions. This limitation put forward a challenge to utilizing bistability to achieve advanced functionality. Therefore, the development of function/application-oriented bistable unit

C. Yue, W. Zhao, F. Li, B. Li, L. Liu, Y. Liu
Department of Astronautical Science and Mechanics
Harbin Institute of Technology
Harbin 150001, China
E-mail: liulw@hit.edu.cn; yj_liu@hit.edu.cn
J. Leng
Center for Composite Materials and Structure
Harbin Institute of Technology
Harbin 150080, China

The ORCID identification number(s) for the author(s) of this article can be found under https://doi.org/10.1002/adfm.202316181

DOI: 10.1002/adfm.202316181

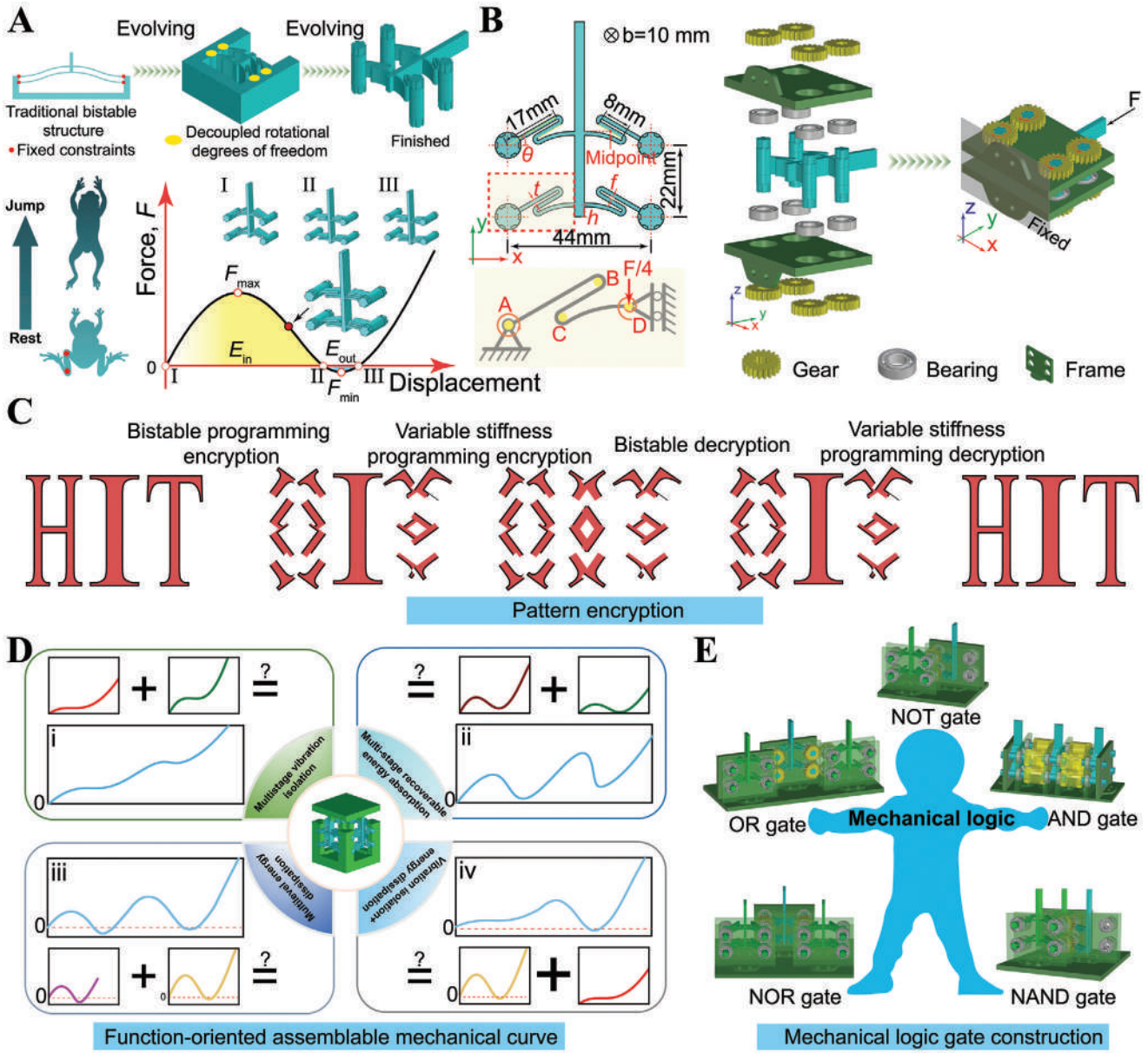

Figure 1. Overview of the unit motif (UM). a) The evolution process and representative force–displacement (*F–D*) curve of bistable UM inspired by frog jumping. b) Geometrical parameters of the designed UM (initially inclined angle θ, thickness t of the arm and gap f), typical simplified deformation diagram of 1/4 UM, and assembly representation with ideal boundary conditions leveraging gear, bearing, and frames. c) The schematic diagram of the pattern encryption function. d) Function-oriented assemblable mechanical performance. e) Construction of mechanical logic gate.

motifs (UMs) is extremely necessary,[40] which is beneficial for truly allocating innovative functions such as pattern encryption devices,[41] programmable friction nanogenerator,[8] sensing/memory devices[12] and logic controller.[28,29,32,42–45]

Rationally fundamental bistable design and combination strategy are reliable solutions to achieve numerous broad and unique mechanical effects and applications. Here, inspired by the hind legs of a frog in the process of jumping, a new unit motif (UM) is developed by introducing rotational degrees of freedom (DOFs) on constraint nodes and two flexible inflection points on the beam (**Figure 1a**). The UMs with different geometrical parameters exhibit snapping behaviors (bistability) and snap-through traits (monostability) with negative incremental stiffness. Figure 1c–e previews three prominent aspects of our work. First, the elegant combinations of variable stiffness materials and proposed UMs offer a research spark. We design a double pattern encryption with the temperature and mechanic switch (Figure 1c). Moreover, the developed assembly strategy provides new opportunities for creating multifunctional metamaterials with demand-assemblable mechanical performance (Figure 1d). Finally, we implement the construction of five non-volatile mechanical logic gates (Figure 1e) and a half adder through the flexible design strategy. The presented design paradigm can guide the exploitation of snap-through instability in the construction of

function-oriented mechanical metamaterials, pattern encryption devices, and electroless machine computing.

2. Results and Discussion

2.1. Design Concept

The proposed UM in our work finds inspiration from the hind leg of the frog in the process of jumping. As seen in Figure 1a, the foot of the frog fits the ground as a flexible pivot point during jumping and the frog has two movable joints on its hind legs. Therefore, our developed UM decouples rotational degrees of freedom on constraint nodes and introduces two flexible inflection points on the beam in comparison with the traditional bistable structure. This offers the unit cell a wider design region and avoids the excessive local peaks in stress. To prevent asymmetric deformation, a double-row beam is designed. Figure 1b shows our UM, which has some fixed dimensions (including a rotation node horizontal spacing of 44 mm, a long arm of 17 mm, and a short arm of 8 mm and more details can be found in Figure S1, Supporting Information) and varying geometrical parameters (initially inclined angle θ, thickness t of the arm and gap f). We take F083010 as an example to explain the nomenclature of UMs. Where "F" in F083010 stands for "LCD" or "FDM,""08" represents $f = 0.8$ mm, "30" signifies $\theta = 30°$, and "10" means $t = 1$ mm. The deformation mode of UM is also showcased in the typical simplified deformation diagram of 1/4 UM in Figure 1b, where point A has only rotational degrees of freedom, points B and C are flexible, and point D is allowed to move in the vertical direction. To meet this movement deformation, we specially design a framework for UMs to test F–D relationships (Figure S2, Supporting Information). The assembly strategy of UMs with ideal boundary conditions leveraging gear, bearing along with frames can be observed in Figure 1b and Video S1, Supporting Information. To have an in-depth understanding on the fundamental mechanics of UM during deformation, we develop a theoretical model of 1/4 UM consisting of pin-connected springs and torsional springs. Section S2, Supporting Information, details the variation of K_2/K_3 values with D_2 in the spring system for the example of FDM082510 and FDM083010. By monitoring the shape of the force-displacement curve obtained from the following equation, we can determine the mechanical behavior of the spring system for different combinations of K_2, K_3, and h.

$$F = \frac{4K_2\left(h-D_2\right)\left(\sqrt{h^2+184}-\sqrt{\left(h-D_2\right)+484}\right)}{\sqrt{\left(h-D_2\right)^2+484}} + \frac{88K_3\left(\tan^{-1}\left(\frac{h}{22}\right)-\tan^{-1}\left(\frac{h-D_2}{22}\right)\right)}{\left(h-D_2\right)^2+484} \quad (1)$$

During compression deformation, the K_3 spring provides a restoring force that always pushes the UM to maintain its initial state; when $0<D_2<h$, the reaction force from the K_2 spring has the same effect as that of the K_3 spring; however when displacement D_2 is beyond h, the direction of the reaction force from the K_2 spring changes, causing a counteraction effect with the K_3 spring, which provides the possibility of new stable states. Figure S3c (Supporting Information) shows that the stiffness of the K_2 and K_3 spring is constantly changing with the loading progress. Numerically, the value of K_2/K_3 changes abruptly near $D_2 = h$, indicating that the magnitude of h has a considerable influence on the variation of K_2/K_3. In Section S3, Supporting Information, we study the effect of structural parameters on the force–displacement curve and energy dissipation of UMs, larger θ and smaller t and f will more easily lead to bistability.

2.2. AMMs with Function-Oriented Mechanical Properties

Next, programmability explorations of metamaterials for performance tuning on-demand are conducted via assembling these UMs and introducing a gradient along the loading direction in the form of 1D chains. Based on the parameterization study of UM, some UMs that meet the requirements are selected. The F–D curves in **Figure 2** show that the experiment and numerical results of the positive stiffness region loaded in the early stage demonstrate good consistency. The reasons for the differences between them may be due to printing accuracy and undesirable friction at rotating nodes. The FEM and experimental results show significant differences in the post-loading stage, especially when the snap-through phenomenon is obvious. A heterogeneous assembly strategy with a gradient can get over the indeterminacy of the deformation sequence. Two low-stiffness platform region during loading corroborates the multistage quasi-static state zero stiffness traits of Sample A. Further, the low stiffness platform can be adjusted through the series and parallel connection of UM. In addition to LCD163016 and FDM143017, the F–D curves with other low-stiffness platforms can also be generated by regulating the geometric parameters of the UM. Figure S10, Supporting Information, gives an analytical nonlinear spring model to represent the corresponding UM with the same F–D response. Focusing on different loads, it is possible to achieve vibration isolation with different amplitudes by combining UMs in series and parallel. Sample B presents two noninitial positive local minimum forces, which facilitate recoverable energy absorption. Sample D displays noticeable snap-back behavior. Moreover, the FEM results of Samples C and D can exhibit two and three stable states respectively, indicating that we can create a reconfigurable and programmable architectural configuration. Due to the dynamic disturbance caused by the snap-through instability during the testing process (Video S3, Supporting Information), the third stable state of sample D cannot be tested through quasi-static experiments, but it still exists through active programming. Similarly, multiple buckling and multistable responses with controllable peak forces can be achieved by utilizing different peak forces and combinations in various buckling dominant UMs. More interestingly, the AMMs assembled by LCD163016 (bottom) and PLACD084016 (top) exhibit both low stiffness platform and snap-through behavior during compression (Figure S12, Supporting Information). In some special application scenarios, such as the launch and recovery of rockets, and the protection of valuables during transportation, this may provide an opportunity for manufacturing equipment that requires both vibration isolation and damping characteristics. More importantly, the flexibility of assembly enables the AMMs

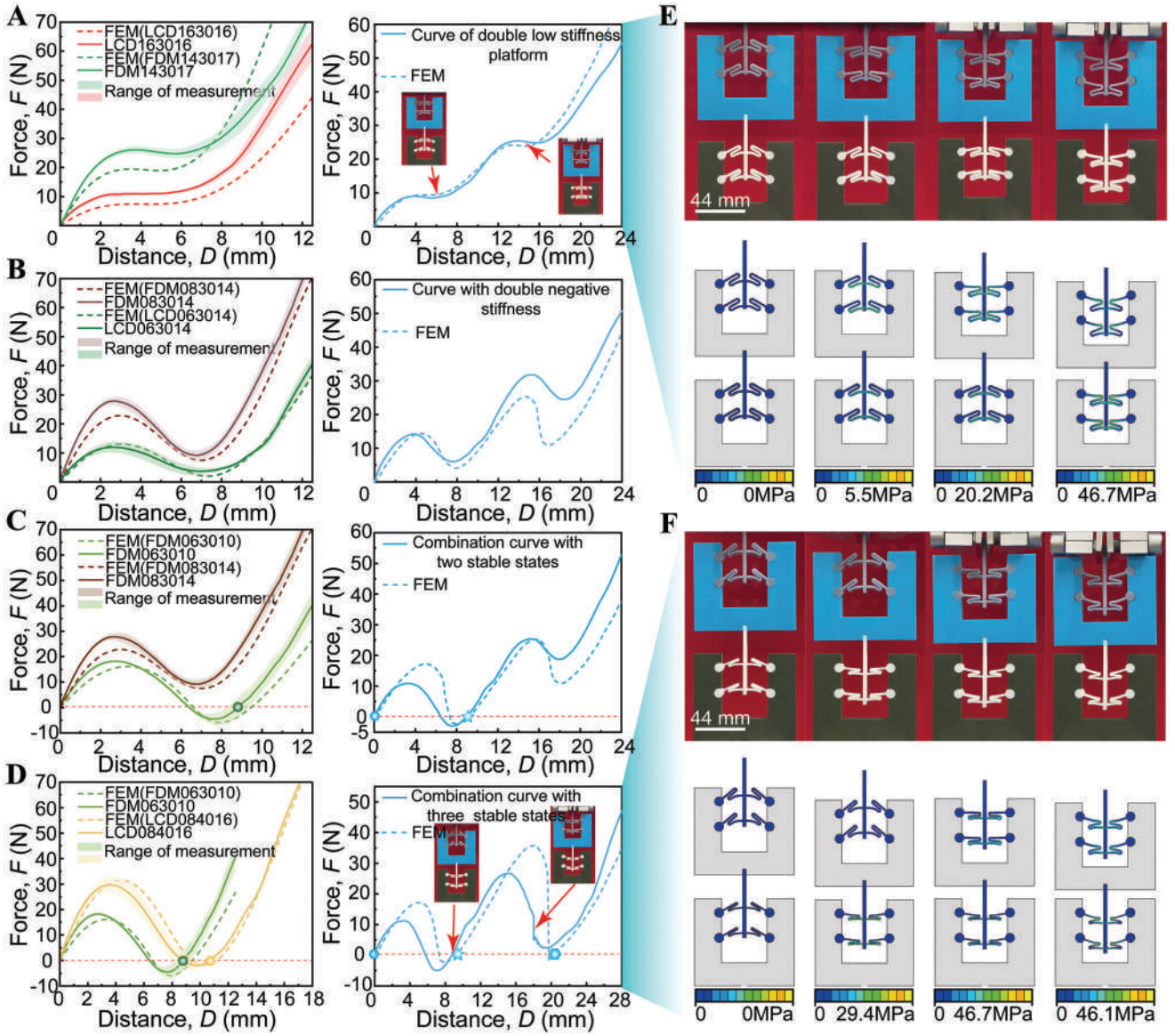

Figure 2. Programmability exploration of metamaterials for performance tailoring on-demand via experimental and finite element methods. a) Mechanical response with double low stiffness platform through assembling LCD163016 (top) and FDM143017 (bottom), which may be used for multi-stage vibration isolation with loads (Sample A). b) Construction of curve with double negative stiffness for creating reusable multi-stage energy absorber in which FDM083014 is below and LCD063014 is upper (Sample B). c) Combination of snapping unit FDM063010 (bottom) and snap-through unit FDM083014 (top) (Sample C). d) A multistable assembly curve with two snapping units which are respectively FDM063010 (bottom) and LCD084016 (top) for producing a damper with energy dissipation function (Sample D). e,f) Experimental snapshots and finite element simulations in a and d (Details of b and c are given in Figure S11, Supporting Information).

to have greater adaptability, rapid scalability, and maintainability. Figure S13, Supporting Information, shows the potential energy of four types of AMMs during loading in Figure 2. Additionally, the compression test under displacement control and the real-time change process of the force–displacement curve can be well observed in Video S3, Supporting Information.

Furthermore, to verify the applicability and scalability of AMMs, we design a 3D assembly scheme and fabricated two 3D AMMs ((i) and (ii)) with repeatable energy absorption performances and multistabilities as depicted in **Figure 3**a,b. The area under the loading curves represents absorbed energy, while the area surrounded by the loading and unloading curves indicates dissipated energy that can be quantified through energy dissipation density (E_d). For sample (i) with 1 × 2 UMs, the structure almost returns to its initial state after unloading, indicating a repeatable deformation mode. Meanwhile, the friction generated at the rotating nodes leads to partial energy dissipation and partial saw-tooth F–D curve. The combined effect of friction and snap-through behavior with negative incremental stiffness produces a large force plateau, demonstrating high energy absorption at an almost constant load (Figure 3a), and its E_d is 985 J m^{-3}. The multistable sample (ii) with 1 × 2 UMs can be

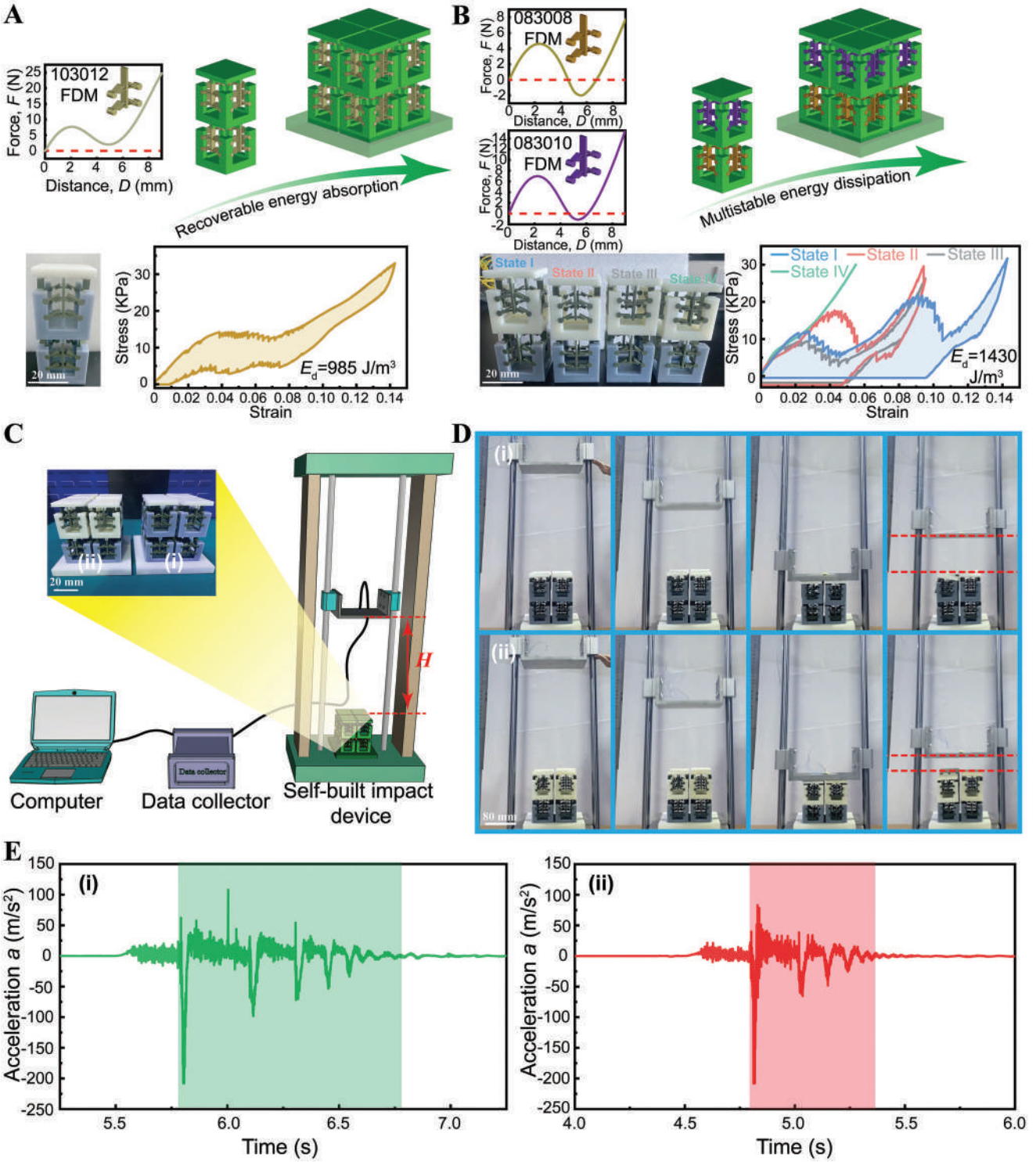

Figure 3. The 3D assembled scheme and application feasibility verification of AMMs. a) Repeatable energy absorbing 3D AMMs and their *F–D* response of loading and unloading under quasi-static. b) 3D AMMs with multistable traits and their *F–D* curves in different stable states at loading/unloading stages under quasi-static. c) Experimental impact testing installation of 3D AMMs with 2 × 2× 2 UMs ((i) Repeatable energy absorbing 3D AMMs and (ii) 3D AMMs with multistable traits) via dropping a plate with a mass of 1500 g from a height of *H* mm. d) Video frames of the drop experiment for (i) and (ii) when *H* = 300 mm (4.41 J impact energy). E) Acceleration response of falling plate for (i) and (ii). In contrast to UMs assembled in the form of 1D chains, all cells of 3D AMMs have been reduced by 0.7 times in size.

configured into four stable states (Figure 3b). Due to the difference between the local maximum force, snaping units FDM083008 and FDM083010 undergo buckling deformation sequentially, which leads to two peaks in the loading path of state I. Remarkably, both two snaping units maintain the second stable state prior to fully unloading, resulting in the large enclosed area between the loading and unloading path, and its E_d is 1430 J m^{-3}. As a result, the specimen has a high energy dissipation during the test process. Comparatively, states II and III display respectively similarly dissipative behavior due to the snaping of FDM083010 and FDM083008 as well as the friction. However, the compression *F-D* relation of State IV is monotonous (Figure 3b). The loading and unloading process of manufactured samples (i) and (ii) with 1 × 2 UMs and their real-time *F–D* response curves are recorded in Video S4, Supporting Information. Section S6, Supporting Information, gives the *F–d* curve of fundamental UMs and the designed demonstration of 3D AMMs with other functional properties. With the development of more advanced additive manufacturing and micro-nanoprocessing technology,[46,47] these complex functional AMMs may be implemented in the future.

In addition, we examine the damping and reusability cushioning performance of the abovementioned 3D AMMs ((i) and (ii)). Self-built drop equipment is used to generate the impact, the details of the equipment and evaluation methods can be found in Figure 3c and the experimental section. Figure 3d,e compares the rebound height and the acceleration response of the impactor dropping on the 3D AMMs from a height of 300 mm (4.41 J impact energy). It can be seen that the rebound height of the impactor for sample (ii) is small with a magnitude of 42.43 mm, and the subsequent impact oscillation due to the re-collision between the impactor and sample is smaller and with a span of 0.61 s. In comparison, the rebound height of the impactor for sample (i) is 98.55 mm, and the subsequent impact oscillation is larger and with a span of 1.04 s. Video S5, Supporting Information, shows more details of the dropping and rebound process of aluminum plates from different heights *H* and the deformation process of samples. Based on the abovementioned discussion, sample (ii) has better buffering performance and damping characteristics than sample (i). However, sample (i) is self-recovering without the need for being pulled back actively.

2.3. AMMs for Pattern Encryption

With the growing importance of pattern information storage and protection, the development of mechanical encryption media with shape-morphing ability, strong robustness, and environmental adaptability has practical significance. Many pattern encryption techniques in fields such as materials science,[48] optics,[49] and mechanics[41,50] have been studied, and our research strategy on mechanical encryption will further supplement and expand the application of pattern encryption. Here, the dual-encryption equipment is engineered and manufactured by leveraging the bistability of the snapping unit and shape memory programmability of the snap-through unit respectively, which affords feasibility for the mechanic and temperature double pattern encryption strategy. Corresponding results for the *F–D* and *φ–D* responses of encryption units and variable stiffness characteristics of snap-through units are separately summarized in **Figure** 4a and Figure S17, Supporting Information. The results show that the storage modulus of printed FDM drops off steeply as the temperature rises, and tan delta data shows that the glass transition temperature of printed FDM is 88 °C. This provides the basis for the temperature encoding of the snap-through unit FDM103014. Figure 4a indicates that the rotation angle of the encrypted unit at rotating nodes gradually increases upon increasing the distance. Besides, the snap-through unit FDM103014 exhibits monostable behavior, and snaping units LCD083010 and FDM084010 are bistable. Their rotation angle *φ* of state II are respectively 36.5° and 53.8°, and greater force is required to move FDM084010 from the state I to state II in comparison with the LCD083010. The deployment location of the encryption units is shown in Figure 4b. Figure 4c and Video S6, Supporting Information, demonstrate the encryption and decryption operations and the status of encryption devices at each stage in detail. First, we compress the snapping units (LCD083010 and FDM083014), and the cropped image is encrypted due to the bistable behavior and nodal rotation. The three times press encryption on the snap-through units (FDM103014) is invalid. Second, the encryption device is placed in hot water above 90 °C, and snap-through units are programmed and encrypted by pressing, which is easier due to their low modulus at high temperatures. After leaving the hot water without removing external forces for cooling, the shape of the programmed snap-through units is fixed because of variable stiffness features, and the encryption process is completed. This process has no impact on the snapping units. It can be observed that the encrypted image is completely different from "HIT." After that, we perform decryption operations by pulling the snaping units, and "H" and "T" are decrypted. Moreover, the operation of pulling snap-through units cannot permanently decrypt "I" at room temperature, and "I" returns to the encrypted state after removing the tension as a result of the monostable behavior of snap-through units. Finally, we permanently reset "I" utilizing hot water. The decrypted image has good consistency with the pre-encrypted image. Furthermore, the encryption operation can be changed from push to pull by inverting the encryption units as shown in Figure S18, Supporting Information. This means that each encryption bit based on the snaping unit and snap-through unit can have four possible encryption or decryption methods, which results in 4^n possibilities for n-bit encryption devices. This strategy offers a reversible and reprogrammable dual-mode pattern encryption-decryption technology, and our device can be reassembled after manufacturing due to the flexibility of the assembly strategy. Meanwhile, any pattern encryption strategy related to other disciplines (such as materials science and optics) can be pasted on the rotating node of encryption units for combined encryption and encoding of different information. More importantly, this has practical significance for the scalability, complexity, and security of encryption and decryption methods in mechanical pattern encryption devices.

2.4. AMMs for Mechanical Logic Gates

In the above pattern encryption research, the encryption units are independent of each other. So what will happen when there are interactivities between UMs? This inspires us to further

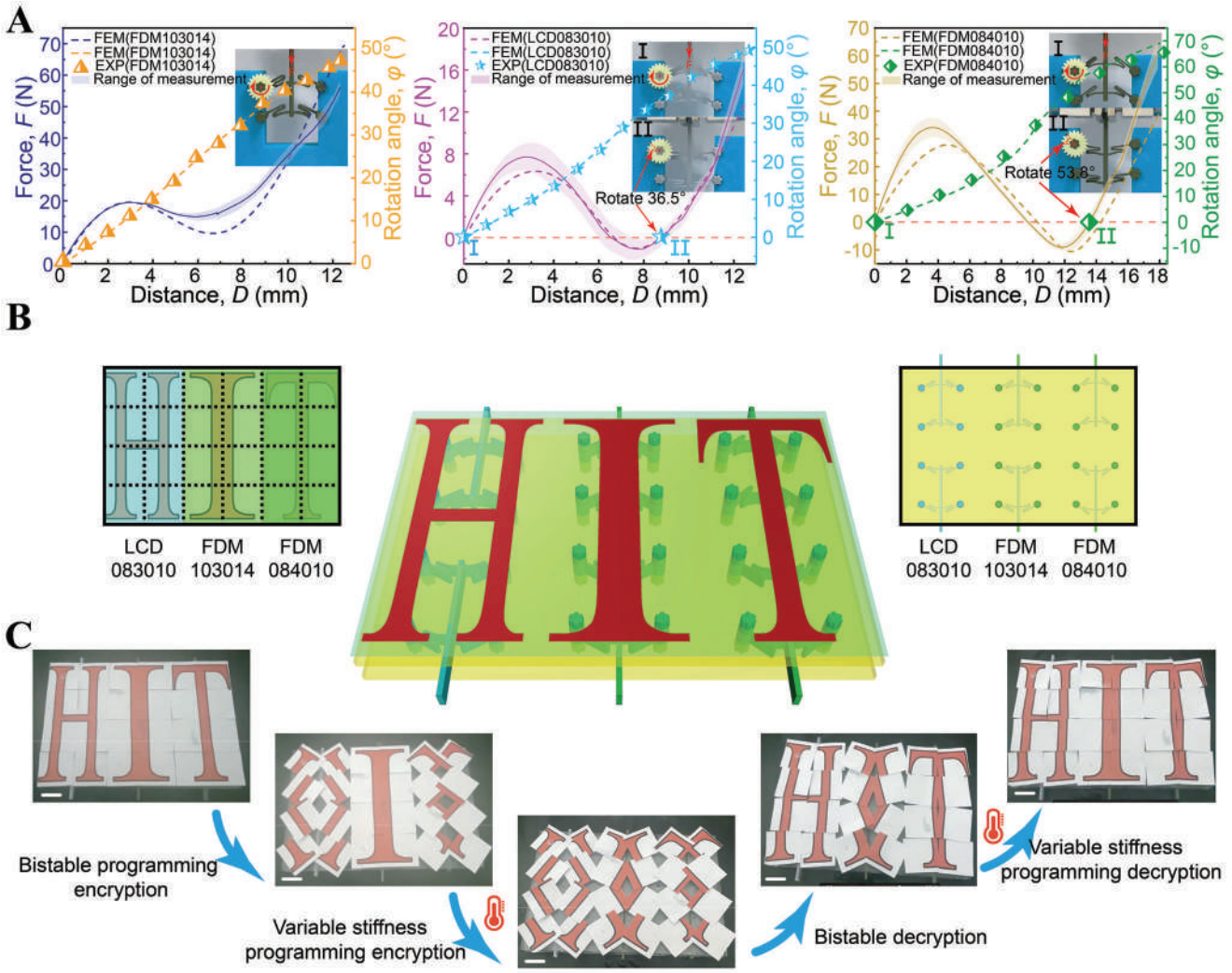

Figure 4. Mechanic and temperature double pattern encryption principles and potential applications demonstration of AMMs. a) Variation of force *F* with displacement and rotation angle φ at the rotational node with displacement (The encryption units are respectively snap-through unit FDM103014 and snapping units LCD083010 and FDM084010). b) Pictures printed with the words HIT and the deployment location of the encryption units. c) Encryption and decryption experimental processes. The scale bar is 22 mm.

research the construction of mechanical logic gates. Mechanical logic gates provide a reliable solution for performing non-electrochemical logic operations in extreme environments such as extremely cold environments, electromagnetic radiation, nuclear radiation, etc.[51] Their performance is more stable and less prone to faults in comparison with electronic logic gates.[52] Here, we build on the snapping UMs to realize five nonvolatile mechanical logic gates including three basic (NOT, AND, and OR) as well as two universal (NAND and NOR) gates as shown in **Figure 5**. The framework with built-in bearings ensures ideal deformation conditions without friction for UMs during logical input and output processes. During the input operation, the input unit relies on the gears at the rotating nodes to transmit force to the output unit. Meshing gears cause the nodes to rotate in opposite directions while sharing gears cause the nodes to rotate synchronously.[53] Section S8, Supporting Information, provides a detailed description of the selection of input units and output units and the detailed exploration process of mechanical logic gates. Figure 5b presents the input operation states and output Boolean responses of the corresponding truth table of five mechanical logic gates, in which the top of the rectangular rod in the middle of the input unit is low, the input signal is 0, otherwise is 1. The output results of 1 and 0 can be monitored by the high and low values at the top of the rectangular rod in the middle of the output unit. The key configuration layouts and descriptions of designed mechanical logic gates can be found in Figure S22 and Section S8, Supporting information. Video S7, Supporting Information, provides the experimental demonstration and the corresponding FEM-predicted computation process, which more intuitively validates the functioning of mechanical logic gates. All logic gates can stably perform three times logical operations as result in Video S7, Supporting Information. Compared to existing research on mechanical logic gates, our method relies entirely on bistability characteristics, does not require any energy to maintain the stable position of the mechanism for stable memory, and this approach may be less

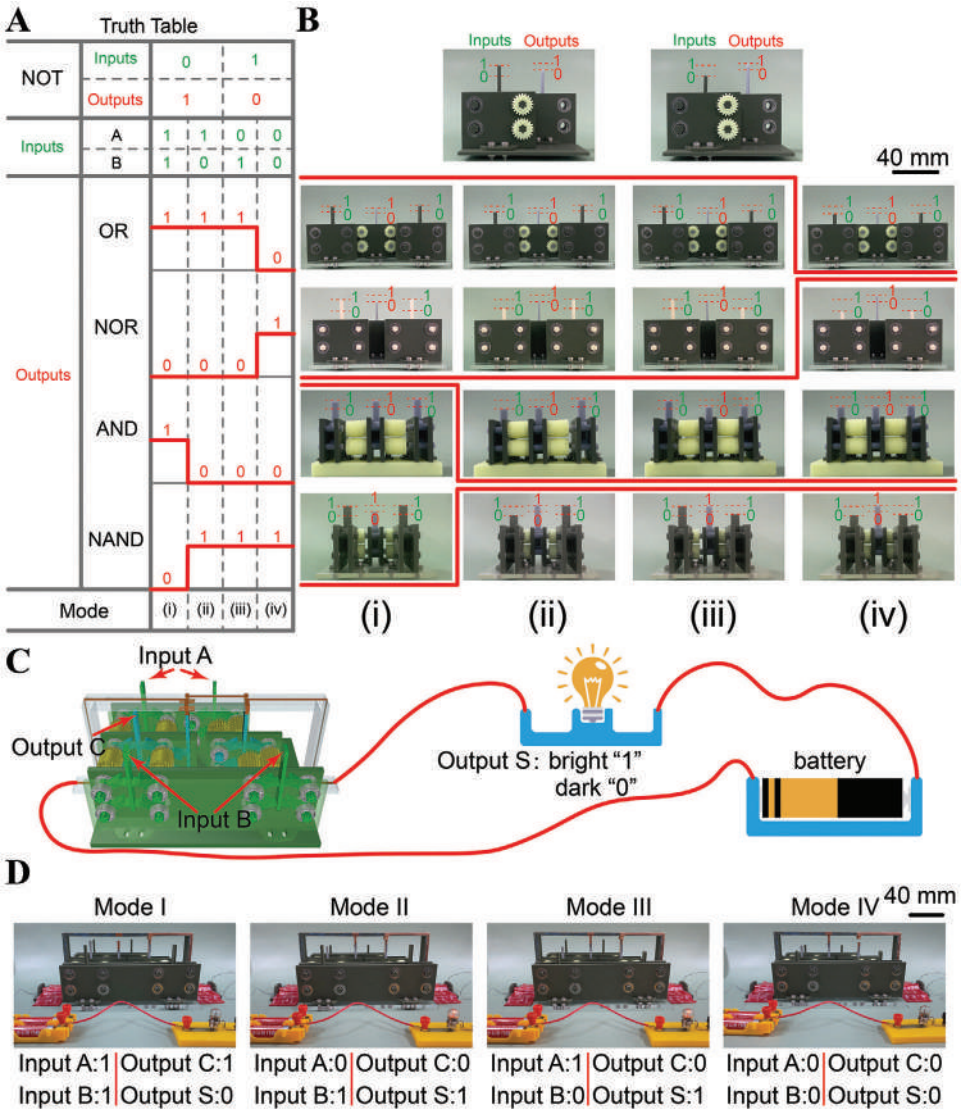

Figure 5. Realization of mechanical logic gates. a) Truth tables of NOT, OR, NOR, AND, and NAND logic operations. b) Experimentally output Boolean response of mechanical logic gate with different logic input modes. c) Schematic diagram of the logic circuit of the half adder. d) The experimental process of implementing logical functions in the half adder.

susceptible to interference. Furthermore, a half adder for calculating the sum of two one-bit binary numbers is created to illustrate the feasibility of combinatorial mechanical logic gates. Figure 5c and Figure S24, Supporting Information, gives the logic circuit and truth tables of the half adder, which has two input ports A and B. The combinatorial half adder consists of a parallel OR gate and AND gate connected in series with NOT gate, as well as the final AND circuit in series. Specifically, the high and low outputs of the mechanical logic AND gate represent "1" and "0" of output C, and the bright and dark of the small bulb indicate the "1" and "0" of output S, respectively. Figure 5d and Video S7, Supporting Information, shows the process of implementing logical functions in the half adder. The results are consistent with the truth tables in Figure S24, Supporting Information. The implementation of a half adder demonstrates the supplement to electronic logic gates, which provides additional confidence for implementing more complex non-volatile mechanical logic functions through our strategy.

3. Conclusion

In summary, we propose a unit motif inspired by the hind leg of the frog in the process of jumping and reported a flexible metamaterial assembly strategy. Such heteroassembly effectively provides a broad range of design space and enables the realization of many function-orient applications, such as buffers, energy absorbers, pattern encryption, and mechanical logic calculations. Based on the UMs with different mechanical properties, we verify the feasibility of assembling mechanical metamaterial with customized mechanical properties through finite element and experimental methods. Moreover, the introduced pattern encryption strategy can realize reversible, reprogrammable, and safer

dual-mode encryption-decryption, and results in increasing encryption and decryption modes exponentially with the encryption elements of mechanical metamaterials. Finally, five basic mechanical logic gates and a combinatorial half-adder are constructed, which can perform non-volatile logic operations well. Going forward, amplified force output,[54] machine learning,[30] or new computing frameworks[31] may be desirable research methods for non-volatile mechanical logic computing. Finally, introducing stimulus response into assembly strategies is one of the pillars of the AMMs research, which would make AMMs more intelligent and potentially boost their mechanical properties.

4. Experimental Section

Design and Fabrication: All snapping units and frames were modeled by Rhino7. The samples were, respectively, manufactured by a fused deposition modeling (FDM) 3D printer (JG Maker, A5S, Shenzhen, China) using poly(lactic acid) (PLA) filaments (eSUN, PLA+) and by Wiiboox UV curing printer (LIGHT TWO PRO, Nanjing, China) using PLA photosensitive resin (eResin-PLA). "LCD" and "FDM" were simplified,respectively. The bearings with model 688zz, conductive copper tape, wires, and electrical experimental teaching aids were all purchased from Taobao. The corresponding 1D and 3D AMMs frameworks were manufactured using FDM and LCD technology, respectively. The acrylic board frames were manufactured to meet the boundary conditions required for the deformation of the encryption units. Meanwhile, the image with the word HIT was cropped according to the back dashed line in Figure 4b and paste them on the rotation node of the encryption unit. The customized mechanical logic gate cellular frameworks and gears (module is 2, number of teeth is 20, and the outside diameter is 20 mm) are fabricated using FDM and LCD technology, respectively.

Sample Characterization: All UMs and AMMs in the form of 1D chains were compressed at a quasi-static rate of 2 mm min^{-1} under displacement control by a Zwick-010 universal testing machine. Cyclic compression tests of the 3D AMMs with 1×2 units were performed at a rate of 5 mm min^{-1}. Impact tests were performed using self-built impact apparatus. An aluminum plate driven by gravity was dropped from different heights H ranging from 50 to 500 mm to impact the samples and the acceleration response of the plate was collected using an acceleration sensor and dynamic data acquisition instrument (Donghua DH5956). Guides and sliders were used to guide the fall of aluminum plates. The total weight of the aluminum plate and two sliders is 1.5 kg. The impact energy, E, can be determined as $E = mgh$. Here, the rebound height is used to evaluate the damping characteristics of the structure, while first peak acceleration and rebound times are used to assess the buffering performance of the structures. The falling process and rebound condition of the plate are captured in the slow-motion mode (720 p and 240 fps) of the camera. All distances and angles in the experiment are measured using the image processing software Image J.

Finite Element Analysis: Implicit dynamic, displacement controlled, and moderate dissipation in the software ABAQUS 6.20 are employed to provide a robust way to simulate the large deformation behavior of UMs and AMMs assembled in the form of 1D chains. The FE simulations use the eight-node hexahedral element with reduced integration (C3D8R) to mesh the model. Base material properties are obtained from the uniaxial tensile experiment of LCD and FDM. Figure S19, Supporting Information, shows that the reference points (RPs) are coupled with the upper and lower surfaces of the rotating nodes of the UM and the upper surfaces of the rectangular bar. The boundary conditions of RPs associated with rotating nodes are $U_1 = U_2 = U_3 = UR_2 = UR_3 = 0$, and that of RP1 is $U_1 = U_3 = UR_1 = UR_2 = UR_3 = 0$. The sensitivity analysis of the grid in Figure S20, Supporting Information, shows that there is little significant difference in the F–D response and φ–d response calculated by grid sizes of 0.2 mm and 0.4 mm. Therefore, a grid size of 0.4 mm is selected to improve computational efficiency. Explicit dynamics is used to simulate the quasi-static process of mechanical logic gate logic input operations.

Supporting Information

Supporting Information is available from the Wiley Online Library or from the author.

Acknowledgements

This work was supported by the National Natural Science Foundation of China (Nos. 12072094 and 12172106).

Conflict of Interest

The authors declare no conflict of interest.

Author Contributions

C.B.Y. and W.Z. contributed equally to this work. C.B.Y. conceived the idea, designed the experiments, carried out the data analysis, and wrote the original manuscript. W.Z. contributed to experimental exploration, part of the impact experiments, finite element analysis, and language modification. F.F.L. contributed to language modification. B.X.L. contributed to part of the impact tests and pattern encryption experiment. L.W.L. contributed to supervision. Y.J.L. and J.S.L. had scientific discussions and improved the manuscript. All authors reviewed and commented on the manuscript.

Data Availability Statement

The data that support the findings of this study are available from the corresponding author upon reasonable request.

Keywords

assembly mechanical metamaterials (AMMs), function-oriented, mechanical logic functions, pattern encryption

Received: December 18, 2023
Revised: March 11, 2024
Published online:

[1] Y. Chi, Y. Li, Y. Zhao, Y. Hong, Y. Tang, J. Yin, *Adv. Mater.* **2022**, *34*, 2110384.
[2] X. Zhang, Y. Wang, Z. Tian, M. Samri, K. Moh, R. M. McMeeking, R. Hensel, E. Arzt, *Sci. Adv.* **2023**, *8*, eadd4768.
[3] Y. Forterre, J. M. Skotheim, J. Dumais, L. Mahadevan, *Nature* **2005**, *433*, 421.
[4] R. Sachse, A. Westermeier, M. Mylo, J. Nadasdi, M. Bischoff, T. Speck, S. Poppinga, *Proc. Natl. Acad. Sci. USA* **2020**, *117*, 16035.
[5] M. L. Smith, G. M. Yanega, A. Ruina, *J. Theor. Biol.* **2011**, *282*, 41.
[6] S. N. Patek, W. L. Korff, R. L. Caldwell, *Nature* **2004**, *428*, 819.
[7] Y. Tang, Y. Chi, J. Sun, T.-H. Huang, O. H. Maghsoudi, A. Spence, J. Zhao, H. Su, J. Yin, *Sci. Adv.* **2020**, *6*, eaaz6912.
[8] C. Huang, T. Tan, Z. Wang, X. Nie, S. Zhang, F. Yang, Z. Lin, B. Wang, Z. Yan, *Nano Energy* **2022**, *103*, 107775.

[9] J. Shi, H. Mofatteh, A. Mirabolghasemi, G. Desharnais, A. Akbarzadeh, *Adv. Mater.* **2021**, *33*, 2102423.
[10] A. Iniguez-Rabago, Y. Li, J. T. B. Overvelde, *Nat. Commun.* **2019**, *10*, 5577.
[11] H. Mofatteh, B. Shahryari, A. Mirabolghasemi, A. Seyedkanani, R. Shirzadkhani, G. Desharnais, A. Akbarzadeh, *Adv. Sci.* **2022**, *9*, 2202883.
[12] T. Chen, M. Pauly, P. M. Reis, *Nature* **2021**, *589*, 386.
[13] J. T. B. Overvelde, T. Kloek, J. J. A. D'haen, K. Bertoldi, *Proc. Natl. Acad. Sci. USA* **2015**, *112*, 10863.
[14] J.-S. Koh, E. Yang, G.-P. Jung, S.-P. Jung, J. H. Son, S.-I. Lee, P. G. Jablonski, R. J. Wood, H.-Y. Kim, K.-J. Cho, *Science* **2015**, *349*, 517.
[15] R. Baumgartner, A. Kogler, J. M. Stadlbauer, C. C. Foo, R. Kaltseis, M. Baumgartner, G. Mao, C. Keplinger, S. J. A. Koh, N. Arnold, Z. Suo, M. Kaltenbrunner, S. Bauer, *Adv. Sci.* **2020**, *7*, 1903391.
[16] T. Frenzel, C. Findeisen, M. Kadic, P. Gumbsch, M. Wegener, *Adv. Mater.* **2016**, *28*, 5865.
[17] K. Fu, Z. Zhao, L. Jin, *Adv. Funct. Mater.* **2019**, *29*, 1901258.
[18] S. Chen, X. Tan, J. Hu, S. Zhu, B. Wang, L. Wang, Y. Jin, L. Wu, *Composites, Part B* **2021**, *215*, 108745.
[19] Y. Chen, L. Jin, *Adv. Funct. Mater.* **2021**, *31*, 2102113.
[20] R. Xu, Y. He, X. Li, M. Lu, Y. Chen, *Appl. Mater. Today* **2023**, *30*, 101714.
[21] Y. Zhang, D. Restrepo, M. Velay-Lizancos, N. D. Mankame, P. D. Zavattieri, *Sci. Rep.* **2019**, *9*, 12581.
[22] S.-Y. Jeon, B. Shen, N. A. Traugutt, Z. Zhu, L. Fang, C. M. Yakacki, T. D. Nguyen, S. H. Kang, *Adv. Mater.* **2022**, *34*, 2200272.
[23] Y. Zhang, M. Tichem, F. van Keulen, *Mater. Des.* **2021**, *212*, 110234.
[24] X. Xia, A. Afshar, H. Yang, C. M. Portela, D. M. Kochmann, C. V. Di Leo, J. R. Greer, *Nature* **2019**, *573*, 205.
[25] B. Haghpanah, L. Salari-Sharif, P. Pourrajab, J. Hopkins, L. Valdevit, *Adv. Mater.* **2016**, *28*, 7915.
[26] Z. Meng, M. Liu, H. Yan, G. M. Genin, C. Q. Chen, *Sci. Adv.* **2023**, *8*, eabn5460.
[27] Y. Liu, F. Pan, B. Ding, Y. Zhu, K. Yang, Y. Chen, *Extreme Mech. Lett.* **2022**, *50*, 101535.
[28] T. Mei, Z. Meng, K. Zhao, C. Q. Chen, *Nat. Commun.* **2021**, *12*, 7234.
[29] H. Zhang, J. Wu, D. Fang, Y. Zhang, *Sci. Adv.* **2023**, *7*, eabf1966.
[30] Z. Liu, H. Fang, J. Xu, K.-W. Wang, *Adv. Intell. Syst.* **2023**, *5*, 2200146.
[31] Z. Liu, H. Fang, J. Xu, K.-W. Wang, *Adv. Sci.* **2023**, *10*, 2305146.
[32] C. El Helou, B. Grossmann, C. E. Tabor, P. R. Buskohl, R. L. Harne, *Nature* **2022**, *608*, 699.
[33] H. Yang, L. Ma, *Mater. Des.* **2020**, *188*, 108430.
[34] X. Tan, S. Chen, B. Wang, S. Zhu, L. Wu, Y. Sun, *Extreme Mech. Lett.* **2019**, *28*, 8.
[35] A. Seyedkanani, A. Akbarzadeh, *Adv. Funct. Mater.* **2022**, *32*, 2207581.
[36] B. Jenett, C. Cameron, F. Tourlomousis, A. P. Rubio, M. Ochalek, N. Gershenfeld, *Sci. Adv.* **2023**, *6*, eabc9943.
[37] S. Shan, S. H. Kang, J. R. Raney, P. Wang, L. Fang, F. Candido, J. A. Lewis, K. Bertoldi, *Adv. Mater.* **2015**, *27*, 4296.
[38] W. Hu, Z. Ren, Z. Wan, D. Qi, X. Cao, Z. Li, W. Wu, R. Tao, Y. Li, *Mater. Des.* **2021**, *200*, 109481.
[39] X. Tan, S. Zhu, B. Wang, K. Yao, S. Chen, P. Xu, L. Wang, Y. Sun, *Composites, Part B* **2020**, *188*, 107898.
[40] Y. Cao, M. Derakhshani, Y. Fang, G. Huang, C. Cao, *Adv. Funct. Mater.* **2021**, *31*, 2106231.
[41] D. Yang, B. Mosadegh, A. Ainla, B. Lee, F. Khashai, Z. Suo, K. Bertoldi, G. M. Whitesides, *Adv. Mater.* **2015**, *27*, 6323.
[42] Y. Song, R. M. Panas, S. Chizari, L. A. Shaw, J. A. Jackson, J. B. Hopkins, A. J. Pascall, *Nat. Commun.* **2019**, *10*, 882.
[43] Z. Meng, W. Chen, T. Mei, Y. Lai, Y. Li, C. Q. Chen, *Extreme Mech. Lett.* **2021**, *43*, 101180.
[44] Y. Jiang, L. M. Korpas, J. R. Raney, *Nat. Commun.* **2019**, *10*, 128.
[45] H. Yasuda, T. Tachi, M. Lee, J. Yang, *Nat. Commun.* **2017**, *8*, 962.
[46] F. Zhang, N. Wen, L. Wang, Y. Bai, J. Leng, *Int. J. Smart Nano Mater.* **2021**, *12*, 375.
[47] Z. Li, X. He, J. Cheng, H. Li, Y.-F. Zhang, X. Shi, K. Yu, H. Y. Yang, Q. Ge, *Int. J. Smart Nano Mater.* **2021**, *12*, 256.
[48] Z. Wang, F. Meng, S. Zhang, Y. Meng, S. Wu, B. Tang, *ACS Appl. Mater. Interfaces* **2020**, *12*, 56413.
[49] J. W. Oh, S. Lee, H. Han, O. Allam, J. Il Choi, H. Lee, W. Jiang, J. Jang, G. Kim, S. Mun, K. Lee, Y. Kim, J. W. Park, S. Lee, S. S. Jang, C. Park, *Light: Sci. Appl.* **2023**, *12*, 226.
[50] X. Hou, F. Vogelbacher, X. Lai, K. Li, Y. Song, M. Li, *Sci. Bull.* **2023**, *68*, 276.
[51] H. Yasuda, P. R. Buskohl, A. Gillman, T. D. Murphey, S. Stepney, R. A. Vaia, J. R. Raney, *Nature* **2021**, *598*, 39.
[52] W. Yan, S. Li, M. Deguchi, Z. Zheng, D. Rus, A. Mehta, *Nat. Commun.* **2023**, *14*, 1553.
[53] X. Fang, J. Wen, L. Cheng, D. Yu, H. Zhang, P. Gumbsch, *Nat. Mater.* **2022**, *21*, 869.
[54] L. Wu, Y. Lu, P. Li, Y. Wang, J. Xue, X. Tian, S. Ge, X. Li, Z. Zhai, J. Lu, X. Lu, D. Li, H. Jiang, *Adv. Sci.* **2023**, *11*, 2308137.